

Tensorial Elastodynamics For Coupled Acoustic/Elastic Anisotropic Media: Incorporating Bathymetry

Harpreet Sethi, Jeff Shragge & Ilya Tsvankin

Center for Wave Phenomena and Dept. of Geophysics, Colorado School of Mines, Golden CO 80401

ABSTRACT

Correctly implementing the fluid/solid boundary conditions at the seafloor is important for accurate full-wavefield imaging and inversion of marine seismic data. Because bathymetric profiles are rarely flat, the associated undulations influence wave modes interacting with the seafloor and, therefore, the ensuing imaging and inversion results. We present a mimetic finite-difference (MFD) approach to solve the equations of anisotropic elastodynamics in a nonorthogonal coordinate system conformal to the bathymetric interface. The vertically deformed coordinate mapping transforms the irregular Cartesian (physical) domain into a regularly sampled generalized computational domain. Fully staggered grids (FSGs) are used to solve the velocity-stress formulation of the anisotropic elastic wave equation. We partition the medium into the acoustic and elastic subdomains and explicitly satisfy the fluid/solid boundary conditions with a split-node approach involving high-order one-sided MFD operators that achieve uniform spatial accuracy throughout the computational domain. The wavefields produced by the tensorial MFD scheme are compared with those from the more computationally expensive spectral-element method to validate our implementation. Numerical examples demonstrate that the MFD+FSG algorithm accurately simulates wavefields even for strongly undulating bathymetric surfaces overlying structurally complex anisotropic media, and does not produce spurious numerical artifacts (e.g., staircasing) or unphysical wave modes often caused by improper handling of the strong-contrast bathymetric interface. The developed MFD+FSG technique can be effectively used as the modeling kernel in a variety of coupled acoustic/elastic imaging and inversion applications.

Key words: acoustic, elastic, coupled, anisotropy, transverse isotropy, mimetic, finite-difference, modeling, multicomponent, bathymetry

1 INTRODUCTION

Modeling seismic wavefields that propagate across irregular interfaces is of practical interest in processing of both marine and land seismic surveys. Handling curved boundaries using regular Cartesian grids remains challenging and gives rise to such numerical artifacts as staircase diffractions. For marine seismic, an additional challenge is accurately handling the fluid/solid boundary in the presence of seafloor bathymetry. The conventional approach - treating the fluid medium as a solid with zero shear-wave velocity - leads to the incorrect boundary conditions and results in inaccurate energy partitioning for body waves, as well as in phase and amplitude distortions for Scholte (de Hoop and Van der Hijden, 1984; Singh et al., 2021) and leaky Rayleigh (Padilla et al., 1999) modes.

A number of numerical and semianalytic methods have been devised to compute elastic wavefields in the presence of an irregular fluid/solid interface. Semianalytic approaches such as the generalized reflection/transmission coefficient method (Ge and Chen, 2007) can be used only for a stack of homogeneous layers separated by irregular interfaces, and the extension to heterogeneous models is challenging to implement. Van Vossen et al. (2002) study a global finite-difference (FD) modeling approach that uses a single elastic wave propagator for a medium composed of fluid and solid layers. They observe errors in the simulated seismo-

grams when the fluid/solid interface is not aligned with the grid; Scholte waves are incorrectly modeled even when the grid and the interface are aligned.

Apart from the noted physical inaccuracy, the computational cost of anisotropic elastic FD solver is approximately five (for 2D) and eight (for 3D) times higher compared to acoustic wave propagators. Thus, it is desirable to use an acoustic wave propagator for the water layer, an elastic propagator for the underlying medium, and then explicitly satisfy the boundary conditions at the fluid/solid bathymetric interface. One strategy to achieve this is to use a partitioned-grid approach where one solves the acoustic wave equation in the fluid and the elastic wave equation in the solid on separate grids that are coupled at the domain boundary (Komatitsch et al., 2000; Käser and Dumbser, 2008; Sun et al., 2017; Singh et al., 2021). Zhang (2004) employs the finite-element method on a partitioned grid for wavefield modeling in the presence of a fluid/solid interface and uses an integral approach to implicitly satisfy the boundary conditions. To compute elastic wavefields for irregular fluid/solid interfaces, Käser and Dumbser (2008) and Wilcox et al. (2010) use discontinuous Galerkin method, whereas Voinovich et al. (2003) employs the finite-volume method. Komatitsch et al. (2000) and Chaljub et al. (2003) develop spectral-element methods to model wave propagation in fluid/solid configurations and achieve the spatial accuracy greater than $O(\Delta x^4)$ [where $O(\Delta x^n)$ denotes the n th-order spatial accuracy]. However, their scheme is computationally expensive and the meshing procedure for creating boundary-conforming grids is complicated. Overall, the algorithmic complexity and computational and memory costs of these high-end techniques prevent their routine application in solving industry-scale 3D anisotropic elastic wavefield modeling and inversion problems.

FD methods are commonly employed along with staggered grids (and their variants) for computing elastic wavefields in industry applications. Key benefits include a straightforward implementation of most FD techniques, compact stencils for computing higher-order derivatives that port well to GPU architectures, and a moderate computational cost, all of which makes them an attractive option for industry-scale applications. The extension of FD methods to curvilinear grids (Fornberg, 1988; Tessmer et al., 1992; Hestholm and Ruud, 1994; Zhang and Chen, 2006; Appelö and Petersson, 2009; Tarrass et al., 2011; de la Puente et al., 2014; Shragge, 2017) makes it possible to handle irregular interfaces and avoid unphysical numerical artifacts (e.g., staircase diffractions). In addition, mimetic FD operators can be used to implement the boundary conditions and boundary stencils with uniform accuracy throughout the entire computational domain (Castillo and Miranda, 2013; de la Puente et al., 2014; Shragge and Konuk, 2020; Singh et al., 2021).

Modeling wave propagation with FD operators across curved bathymetric surfaces can be implemented by solving the governing wave equations directly on the deformed grids conformal to interfaces using a chain-rule approach that transforms the partial wavefield derivatives from curvilinear to Cartesian coordinates (Hestholm and Ruud, 1994; de la Puente et al., 2014; Sun et al., 2017). However, this methodology is computationally expensive because it requires additional partial-derivative calculations (Komatitsch et al., 1996). Alternatively, wave equations can be solved directly on curved grids using a tensorial formulation that is independent of a coordinate system. This approach involves computing the same number of partial wavefield derivatives as that required for Cartesian coordinate solutions. However, additional memory is needed to store the geometry-related fields (Komatitsch et al., 1996), unless one follows the semianalytic formulation of Shragge and Konuk (2020) for vertically deformed meshes. The tensorial approach has been developed for elastic isotropic (Komatitsch et al., 1996; Shragge and Konuk, 2020) and anisotropic models with free-surface topography (Konuk and Shragge, 2019); however, we are unaware of any applications involving coupled media in the presence of irregular bathymetry.

In this paper, we present a novel contravariant formulation of tensorial elastodynamics that extends the approach of Shragge and Konuk (2020) to coupled acoustic/elastic models with bathymetry. We partition the medium into the fluid and solid subdomains and solve the respective acoustic and elastic wave equations using MFD operators on fully staggered grids (FSG). The two subdomains are coupled at the internal bathymetric interface by satisfying the fluid/solid boundary conditions with a split-node approach (Singh et al., 2021). First, we review the tensorial theory of acousto- and elastodynamics and the boundary conditions for a fluid/solid interface. Then we present an analytic description of the generalized family of vertically deformed coordinate systems and specify a particular coordinate mapping based on quadratic Bézier interpolants that automatically maps bathymetry to a surface-conforming grid. Next, we discuss the numerical implementation of the proposed technique including the application of the MFD+FSG approach to incorporate the fluid/solid boundary conditions. Numerical examples for 2D models with curvilinear fluid/solid interfaces illustrate the accuracy of our tensorial MFD method for both isotropic and anisotropic elastic media.

2 THEORY

The coupled acoustic/elastic MFD+FSG approach for complex bathymetry involves tensorial representations of acousto- and elastodynamics and implementation of the fluid/solid boundary conditions at the bathymetric interface. The tensorial approach operates in a generalized but uniformly sampled 2D coordinate system ξ that represents the model in the computational domain. The gener-

alized coordinate system is related to an underlying Cartesian mesh \mathbf{x} that represents the model in physical space. The two domains are connected via smooth and invertible forward and inverse transformations, $\xi^i = \xi^i(\mathbf{x})$ and $x^i = x^i(\boldsymbol{\xi})$. The reader is referred to Appendix A for a review of the tensorial calculus used in the development of our tensorial MFD approach. Shragge and Tapley (2017) and Shragge and Konuk (2020), respectively, present more complete developments of tensorial acousto- and elastodynamics.

2.1 Tensorial elastodynamics

The tensorial formulation of elastodynamics involves specifying three governing equations: (1) conservation of linear momentum; (2) a stress-strain constitutive relationship; and (3) an infinitesimal strain-displacement approximation. The first equation is for conservation of linear momentum in a heterogeneous anisotropic elastic medium which can be written in the contravariant form (Brillouin and Brennan, 1965; Flügge, 1972; McConnell, 2014):

$$\rho_s \dot{v}^i = \nabla_j \sigma^{ij} + f^i, \quad (1)$$

where ρ_s is the density, v^i is the i th contravariant component of the particle-velocity vector, a dot above a variable denotes the temporal derivative, σ^{ij} is the second-order contravariant stress tensor, and f^i is the contravariant body force per unit volume. Throughout the manuscript we assume the summation convention; the indices range over $i, j = 1, 2$ for the 2D implementation presented here. The covariant derivative ∇_j of the contravariant stress tensor σ^{ij} in equation 1 can be expanded as

$$\nabla_j \sigma^{ij} = \sigma^{ij}_{,j} + \Gamma_{jl}^i \sigma^{lj} + \Gamma_{jl}^j \sigma^{il}, \quad (2)$$

where $\sigma^{ij}_{,j}$ represents the partial derivative of σ^{ij} with respect to x^j , and Γ_{jl}^i are the Christoffel symbols of the second kind, which are defined in equation A.4 using the metric tensor g_{ij} (equation A.1).

The second equation is the linear constitutive relationship (i.e., Hooke's law) linking the contravariant stress- and covariant strain-rate tensors, $\dot{\sigma}^{ij}$ and $\dot{\epsilon}_{kl}$, through

$$\dot{\sigma}^{ij} = C^{ijkl} \dot{\epsilon}_{kl}, \quad (3)$$

where C^{ijkl} is the fourth-order contravariant stiffness tensor.

Finally, assuming infinitesimal displacements (i.e., $\nabla_l v_k \ll 1$) allows us to write the third governing equation as

$$\dot{\epsilon}_{kl} = \frac{1}{2} (\nabla_l v_k + \nabla_k v_l) = \frac{1}{2} (v_{,l}^k + v_{,k}^l) - \Gamma_{kl}^i v_i, \quad (4)$$

where v_k and v_l are the covariant components of the particle-velocity vector; note that we have exploited the symmetry properties of the Christoffel symbols (i.e., $\Gamma_{kl}^i = \Gamma_{lk}^i$).

In this representation of elastodynamics, all fields retain the well-known tensorial symmetry properties (i.e., $\sigma^{ij} = \sigma^{ji}$, $\epsilon_{kl} = \epsilon_{lk}$, $C^{ijkl} = C^{jikl} = C^{jilk} = C^{ijlk} = C^{klij}$), which yield a maximum of 21 independent stiffness coefficients for the most general (triclinic) anisotropy. Finally, the relationship between the covariant particle-velocity components in equation 4 and the contravariant components in equation 1 can be established using the rank-one tensor index-raising operation (equation A.6).

2.2 Tensorial acoustodynamics

The equations of motion in an inviscid fluid are governed by the conservation of linear momentum and mass. For a generalized coordinate system, these equations can be written as

$$\rho_f \dot{v}_f^i + g^{ij} \frac{\partial p}{\partial \xi^j} = 0 \quad (5)$$

and

$$\dot{p} + \rho_f c_f^2 \nabla_i v_f^i = 0, \quad (6)$$

where p is the pressure, ρ_f is the fluid density, c_f is the fluid velocity, v_f^i is the covariant component of the particle velocity, and g^{ij} is the contravariant metric tensor defined by equation A.2. The covariant derivative of the contravariant vector is defined in equation A.15.

2.3 Fluid/solid boundary conditions

The boundary conditions coupling acoustic and elastic media are the continuity of traction and of the normal component of the particle velocity, also known as the dynamic and kinematic boundary conditions, respectively. The continuity of traction is given by

$$\sigma^{ij} n_j = -p I^{ij} n_j, \quad (7)$$

where I^{ij} is the unit contravariant tensor, p is pressure and \mathbf{n} is the unit vector normal to the surface. The continuity of the normal component of the particle velocity is expressed as

$$v_i^f n_i = v_i^s n_i. \quad (8)$$

Note that equations 7 and 8 form a system of equations for an irregular fluid/solid interface because, in contrast to the flat seafloor case, the normal \mathbf{n} does not necessarily point in the vertical direction.

The boundary condition at the top of the acoustic layer (i.e., at the water-air interface) requires setting

$$p = 0 \quad (9)$$

for all nodes located on the free surface.

3 VERTICALLY DEFORMED COORDINATE SYSTEMS

One of the challenges in generating FD solutions on curvilinear grids is choosing an optimal coordinate mapping. While there are numerous approaches to creating meshes, herein we use a family of nonorthogonal coordinate transformations that allows computational grids to be specified *implicitly* using minimal information about the controlling surfaces. This approach reduces memory requirements because one does not need to hold any coordinate system of geometric field in memory beyond the bathymetric profile itself. The resulting meshes are deformed only in the vertical (depth) direction ξ^1 , but effectively remain Cartesian in the lateral direction ξ^2 .

The family of 2D vertically deformed coordinate systems (Shragge and Tapley, 2017; Shragge and Konuk, 2020) is defined by:

$$\mathbf{x} = \begin{bmatrix} x^1 \\ x^2 \end{bmatrix} = \begin{bmatrix} F(\xi^1, \xi^2) \\ \xi^2 \end{bmatrix}, \quad (10)$$

where $F(\xi^1, \xi^2)$ is a generalized function representing vertical deformation, an example of which is presented below.

As discussed above, the tensorial wave equation includes the inverse metric tensor g^{ij} , the determinant of the metric tensor $|g|$, and the Christoffel symbols of the second kind Γ_{jl}^i . For the transformation in equation 10, the inverse metric tensor is:

$$g^{ij} = \frac{1}{F_1} \begin{bmatrix} F_1^{-1}(1 + F_2^2) & -F_2 \\ -F_2 & 1 \end{bmatrix}, \quad (11)$$

where F_i represents the partial derivative of F with respect to x^i . The square root of the metric tensor determinant $\sqrt{|g|}$ is:

$$\sqrt{|g|} = F_1. \quad (12)$$

The associated Christoffel symbols of the second kind are:

$$\begin{bmatrix} \Gamma_{jk}^1 \\ \Gamma_{jk}^2 \end{bmatrix} = \frac{1}{F_1} \begin{bmatrix} F_{j,k} \\ 0 \end{bmatrix}, \quad (13)$$

where $F_{j,k}$ represents a second-order partial derivative.

Herein, we generate an analytic coordinate system based on quadratic Bézier interpolation that uses three control interfaces (see Appendix B for details). We use a bathymetric surface regularly sampled in the lateral direction that is described in a parametric form for 2D problems as $B(\xi^2)$. The employed mapping defines the undulating bathymetry in the Cartesian coordinate system corresponding to the physical domain \mathbf{x} . The irregular physical mesh is mapped to a regular computational mesh (where bathymetry behaves as a flat surface) in the generalized coordinate system ξ corresponding to the computational domain. To generate a C^2 -diffeomorphic (i.e., smooth, differentiable, and invertible) mesh, we use quadratic Bézier interpolants that pass through three control interfaces: (1) the free surface $x^1 = \xi^1 = 0$; (2) the bathymetry profile $B(\xi^1 = \zeta, \xi^2)$ where ζ is the seafloor location on the grid, and (3) a flat layer at depth $x^2 = \xi^2 = a$ where a is the bottom of the model (maximum depth). For these constraints, the 2D

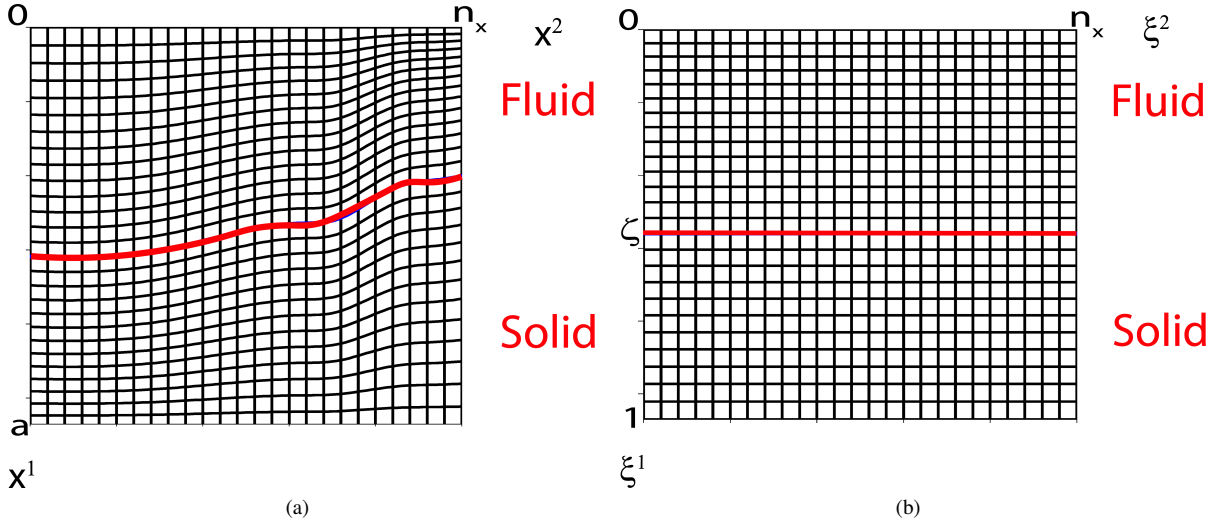


Figure 1. Illustration of the coordinate mapping. (a) The physical Cartesian coordinate system. (b) The generalized regularly sampled computational mesh. The thick red lines mark the bathymetric surface defined at the coordinate level $\xi^1 = \zeta$ and mapped to flat layers in the computational mesh.

vertically deformed coordinate transformation may be expressed as

$$\begin{bmatrix} x^1 \\ x^2 \end{bmatrix} = \begin{bmatrix} \xi^1 (B(\xi^1 - 1) + a\zeta(\zeta - \xi^1)) \\ \zeta(\zeta - 1) \xi^2 \end{bmatrix}. \quad (14)$$

Figure 1 shows the mapping of a mesh in the physical coordinate system (Figure 1a) to a uniformly sampled grid in the computational domain (Figure 1b) using the quadratic Bézier curves.

The coordinate mapping in equation 14 leads to the following covariant metric tensor g_{ij} :

$$g_{ij} = \begin{bmatrix} \frac{(a\zeta(\zeta - 2\xi^1) + (2\xi^1 - 1)B)^2}{\zeta^2(\zeta - 1)} & \frac{\xi^1(\xi^1 - 1)(a\zeta(\zeta - 2\xi^1) + (2\xi^1 - 1)B)B'}{\zeta^2(\zeta - 1)} \\ \frac{\xi^1(\xi^1 - 1)(a\zeta(\zeta - 2\xi^1) + (2\xi^1 - 1)B)B'}{\zeta^2(\zeta - 1)^2} & 1 + \left(\frac{\xi^1(\xi^1 - 1)B'}{\zeta(\zeta - 1)}\right)^2 \end{bmatrix}, \quad (15)$$

where B' is the derivative of the bathymetric surface. The associated contravariant metric tensor is:

$$g^{ij} = \begin{bmatrix} ((\xi^1 - 1)\xi^1 B')^2 + (\zeta - 1)^2 \zeta^2 \gamma^2 & (\xi^1 - 1)\xi^1 B' \gamma \\ (\xi^1 - 1)\xi^1 B' \gamma & 1 \end{bmatrix}, \quad (16)$$

where $\gamma = [a\zeta(2\xi^1 - \zeta) + B(1 - 2\xi^2)]^{-1}$. Finally, the three independent Christoffel symbols Γ_{11}^1 , Γ_{21}^1 and Γ_{22}^1 are given by:

$$\Gamma_{11}^1 = 2(a\zeta - B)\gamma, \quad (17)$$

$$\Gamma_{21}^1 = (1 - 2\xi^1)B'\gamma, \quad (18)$$

$$\Gamma_{22}^1 = \xi^1(1 - \xi^1)B''\gamma. \quad (19)$$

The vector \mathbf{n} normal to the bathymetric surface can be computed as:

$$\mathbf{n} = \frac{1}{|\mathbf{n}|} \begin{bmatrix} 1 \\ -B' \end{bmatrix}, \quad (20)$$

where $|\mathbf{n}| = \sqrt{1 + (B')^2}$. These are all geometric objects required in the tensorial acousto- and elastodynamics defined above. Note that these fields depend solely on the bathymetric surface B and its derivatives B' and B'' . Thus, there is a negligible memory overhead associated with the coordinate mapping and geometric variables.

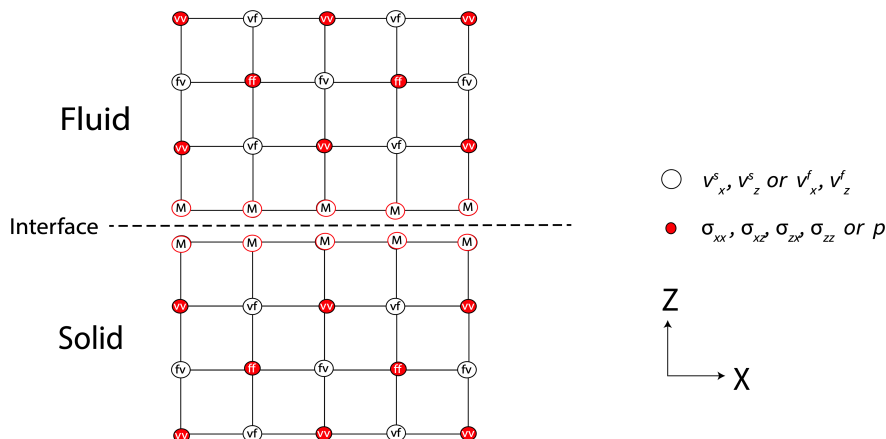


Figure 2. 2D nodal distribution near a fluid/solid interface. The open circles in the fluid and solid correspond to v_i^f and v_i^s , respectively, defined on the $[\mathbf{f}, \mathbf{v}]$ and $[\mathbf{v}, \mathbf{f}]$ grids. The red points in the fluid and solid correspond to p and σ_{ij} defined on the $[\mathbf{f}, \mathbf{f}]$ and $[\mathbf{v}, \mathbf{v}]$ grids.

4 NUMERICAL IMPLEMENTATION

In this section we review the split-domain MFD+FSG approach described in Singh et al. (2021) for coupled acoustic/elastic media with flat bathymetry and Cartesian grids. Much of the implementation framework herein is similar to the one presented in Singh et al. (2021); thus, in this section we focus mainly on the details required to implement the bathymetric surface.

The split-domain MFD+FSG approach involves dividing the model into two computational subdomains corresponding to the fluid and solid media (see Figure 2) and defining a set of interface grid points on either side of the fluid/solid interface. Figure 2 also shows the mimetic points (defined at collocated points on both sides of the fluid/solid interface), which are used for updating the field variables. We discuss how they are used to implement the fluid/solid boundary conditions in the next subsection. For each subdomain we define a 2D FSG system, equivalent to two coupled standard staggered grids (SSGs) with complementary grid staggerings shifted by half-grid spacing in the horizontal and vertical directions. The discretized pressure p and stress σ_{ij} fields are defined at $[\mathbf{f}, \mathbf{f}] \in \mathbb{R}^{(N+2) \times (N+2)}$ and $[\mathbf{v}, \mathbf{v}] \in \mathbb{R}^{(N+1) \times (N+1)}$ formed by two $[\mathbf{f}, \mathbf{f}]$ and $[\mathbf{v}, \mathbf{v}]$ grid nodes, respectively. The discretized particle velocities are defined at $[\mathbf{f}, \mathbf{v}] \in \mathbb{R}^{(N+2) \times (N+1)}$ and $[\mathbf{v}, \mathbf{f}] \in \mathbb{R}^{(N+1) \times (N+2)}$ formed by two $[\mathbf{f}, \mathbf{v}]$ and $[\mathbf{v}, \mathbf{f}]$ grid nodes, respectively.

We use mimetic divergence and gradient operators \mathbf{D} and \mathbf{G} of $O(\Delta x^4)$ spatial accuracy to compute the wavefield derivatives in equations 1-6 (Singh et al., 2021). The mimetic gradient operator \mathbf{G} acts only on the field variables defined on the \mathbf{f} -grid and maps them to form the vector defined on the \mathbf{v} -grid. The mimetic divergence matrix operator \mathbf{D} acts only on the field variables defined on the \mathbf{v} -grid and maps them to form the vector defined on the \mathbf{f} -grid. In 2D MFD FSG, the \mathbf{D} and \mathbf{G} operators act in both the ξ^1 - and ξ^2 -directions in a cyclic fashion (Singh et al., 2021). For example, to compute the derivative along the ξ^1 -direction of σ_{ij} defined on the $[\mathbf{f}, \mathbf{f}]$ grid, one needs to apply a mimetic gradient operator \mathbf{G} that contributes the resulting derivative to v_i defined on the $[\mathbf{v}, \mathbf{f}]$ grid. For further details, the reader is referred to Shragge and Tapley (2017) and Singh et al. (2021).

The MFD+FSG approach requires applying appropriate weighting for source injection and wavefield extraction due to intertwining of multiple grids (Lisitsa and Vishnevskiy, 2010). We perform both injection and extraction in the generalized coordinate system, so first the field variables need to be transformed from the Cartesian system to the generalized coordinate system. This transformation for the force vector is defined in equation A.7. Likewise, for velocity wavefield extraction, the particle-velocity vector can be transformed back to the Cartesian coordinate system using equation A.10, and then sinc-interpolated to a regularly sampled output mesh for visualization purposes (Shragge, 2017). We apply the convolutional perfectly matched layer (C-PML) boundary condition (Martin et al., 2008) at all sides of the model except for the free surface.

4.1 Fluid/solid interface FSG implementation

We implement the fluid/solid boundary conditions using a strategy similar to that described in Singh et al. (2021). The particle-velocity vectors v^s (in the solid subdomain) and v^f (in the fluid subdomain) defined on the $[\mathbf{v}, \mathbf{f}]$ and $[\mathbf{v}, \mathbf{v}]$ grids at the split-node interface are locally rotated into a Cartesian coordinate system where one axis is oriented normal to the bathymetric surface. The normal component of the particle-velocity vector is then replaced by $(v_N^s + v_N^f)/2$, where v_N^s and v_N^f are the normal components of the particle-velocity vector in the solid and fluid, respectively after the rotation. Similarly, the normal component of stress is

Step	Substep	Instruction	Equation(s)
0		Initialize $v^i(\boldsymbol{\xi})$, $p(\boldsymbol{\xi})$, and $\sigma^{kl}(\boldsymbol{\xi})$	—
1		For all time steps:	—
2		Update $p(\boldsymbol{\xi})$	6
3		Update $v_f^i(\boldsymbol{\xi})$	5
4		Apply PML in fluid subdomain	—
5		Apply free-surface boundary condition	13
6		Update strain tensor	—
	6a	Lower index $v^i(\boldsymbol{\xi}) \rightarrow v_i(\boldsymbol{\xi})$	A.6
	6b	Compute $\epsilon_{kl}(\boldsymbol{\xi})$	6
7		Update stress tensor	—
	7a	Transform $\epsilon_{kl}(\boldsymbol{\xi}) \rightarrow \epsilon_{kl}(\boldsymbol{x})$	A.13
	7b	Compute $\sigma^{kl}(\boldsymbol{x})$	5
	7c	Transform $\sigma^{kl}(\boldsymbol{x}) \rightarrow \sigma^{kl}(\boldsymbol{\xi})$	A.4 / A.12
8		Raise index $v_i(\boldsymbol{\xi}) \rightarrow v^i(\boldsymbol{\xi})$	1
9		Inject force source $f^i(\boldsymbol{\xi})$ into $v^i(\boldsymbol{\xi})$	7
10		Apply PML in the solid subdomain	—
11		Apply fluid/solid boundary conditions	—
	11a	Transform $v^i(\boldsymbol{\xi}) \rightarrow v^i(\boldsymbol{x})$ and $\sigma^{kl}(\boldsymbol{\xi}) \rightarrow \sigma^{kl}(\boldsymbol{x})$ along bathymetry profile	A.10 / A.13
	11b	Enforce dynamic and kinematic boundary conditions	7 / 8
	11c	Transform $v^i(\boldsymbol{x}) \rightarrow v^i(\boldsymbol{\xi})$ and $\sigma^{kl}(\boldsymbol{x}) \rightarrow \sigma^{kl}(\boldsymbol{\xi})$ along bathymetry profile	A.7 / A.12
12		Iterate steps 1-11	—

Table 1. Pseudocode that outlines the main steps of the MFD+FSG numerical solution along with the relevant equations.

replaced by $(\sigma_{NN}^s - p)/2$, where σ_{NN}^s is the value after rotation. The resulting field variables are then rotated back into the Cartesian coordinate system and further transformed to the generalized coordinate system to update the mimetic points shown in Figure 2. This incurs an additional but moderate computational cost of rotating the field variables along the bathymetric surface, applying the boundary conditions, and transforming the field variables back to the Cartesian and then to the generalized coordinate system. For the $[\mathbf{f}, \mathbf{f}]$ and $[\mathbf{f}, \mathbf{v}]$ sets of nodes, we use the tensorial acoustic and elastic wave equations to update the mimetic points along with the boundary conditions (equations 7 and 8) using the approach described in Singh et al. (2021).

4.2 Pseudocode for numerical solution

Table 1 presents a pseudocode for our numerical implementation of the tensorial MFD+FSG algorithm. Steps 2-5 pertain to updating the acoustodynamics solution in the fluid subdomain, steps 6-10 are for updating the elastodynamics solution in the solid subdomain, and step 11 enforces the fluid/solid boundary conditions. Note that we update the stiffness tensor in step 7 in a Cartesian coordinate system to avoid representing C^{ijkl} in a nonorthogonal coordinate system where the stiffness tensor may become fully populated even for VTI media. A pragmatic approach is to apply Hooke's law in the Cartesian coordinate system and transform the resulting stress tensor back to the generalized coordinate system. This can be done through several floating-point calculations with minimal computational overhead.

5 NUMERICAL EXAMPLES

We test the developed algorithm for models with a fluid/solid interface including both isotropic and anisotropic solids. The resulting solutions are compared with the spectral-element method (SEM) (Komatitsch and Vilotte, 1998) to validate the algorithm.

First, we consider a bathymetric surface that represents a sinusoidal function of the lateral x^2 -coordinate with the maximum undulations of ± 40 m. The medium beneath the surface is elastic and isotropic (Figure 3). The model size is 100×100 with a grid spacing of $\Delta\xi^1 = \Delta\xi^2 = 10$ m. A 10 Hz Ricker wavelet is injected just above the interface at $[x^1, x^2] = [496, 500]$ m. The simulation progresses for 2500 time steps of $\Delta t = 0.0025$ s. Figure 3 presents the wavefield snapshots of the velocity component v_z at four different simulation times. The panels show different modes including reflected and transmitted P- and S-waves, as well as head and surface (Scholte) waves. The numerical simulation is stable and reconstructs all expected arrivals. To validate our algorithm, the simulation results are compared in Figure 4 with those produced by the spectral-element method (Komatitsch

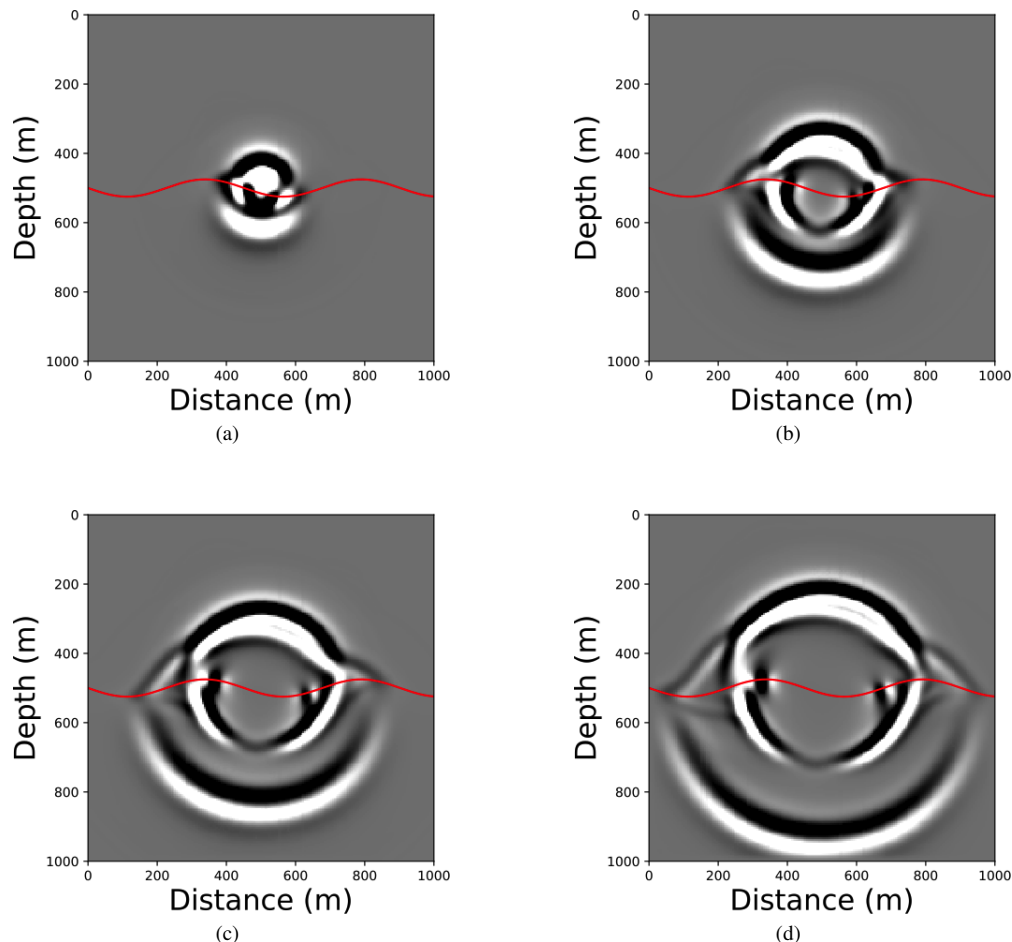


Figure 3. Snapshots of the Cartesian particle-velocity component v_z at (a) $t=0.15$ s, (b) $t=0.2$ s, (c) $t=0.4$ s, and (d) $t=0.45$ s. The bathymetric surface (red) separates the fluid (top) and isotropic solid (bottom) subdomains. The elastic medium is defined by $V_P = 2.5$ km/s, $V_S = 1.2$ km/s, and density $\rho_S = 2.0$ g/cm³. The velocity and density in the fluid are $c_f = 1.5$ km/s and $\rho_f = 1.0$ g/cm³, respectively.

and Vilotte, 1998). The excellent agreement between the two solutions confirms that the tensorial approach combined with the MFD+FSG implementation outlined in Table 1 produces accurate results for curved bathymetric surfaces.

For the second example, we consider a tilted bathymetric surface that separates the upper acoustic subdomain from a transversely isotropic medium with a vertical symmetry axis (VTI). The model size is 100×100 with a grid spacing of $\Delta\xi^1 = \Delta\xi^2 = 10$ m. A 10 Hz Ricker wavelet is injected in the acoustic medium at $[\xi^1, \xi^2]=[496, 500]$ m. Figure 5 presents snapshots of the v_z -component, which again include body and surface waves, whose propagation is strongly influenced by the shape of the boundary. Note that the kinematics of the wavefield propagating in the solid is clearly influenced by velocity anisotropy. The agreement between our and SPECFEM2D solutions confirms the accuracy of the developed method, this time for an anisotropic medium (Figure 6).

For the third and final test, we apply the algorithm to a heterogeneous Hess VTI model with the Thomsen parameters V_{P0} , V_{S0} , ϵ and δ shown in Figure 7. The solid VTI subdomain is separated from the acoustic subdomain by the shallow bathymetry profile. The model size is 250×250 with the grid spacing $\Delta\xi^1 = \Delta\xi^2 = 4$ m. We inject a 25 Hz source wavelet at $[x^1, x^2]=[50, 500]$ m. The results in Figure 8 demonstrate that our algorithm can model numerically stable, complex wavefields for vertically and laterally heterogeneous anisotropic media beneath an undulating bathymetric surface.

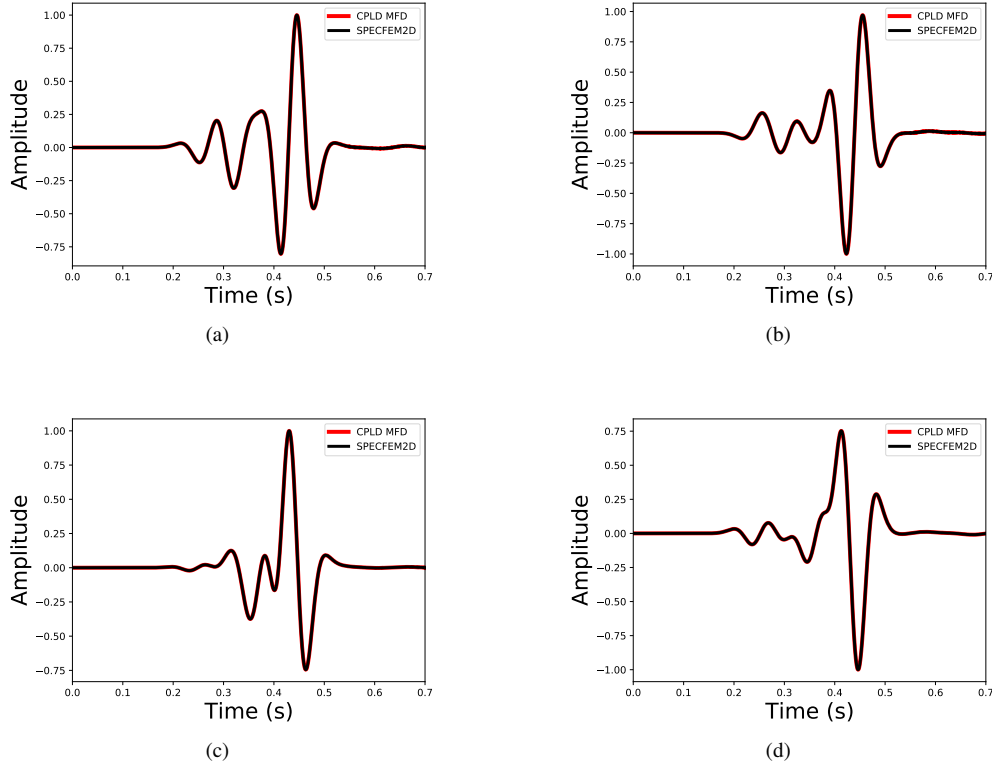


Figure 4. Normalized seismograms for the model in Figure 3. The red and black lines mark the coupled-domain MFD (CPLD MFD) and spectral-element (SPECFEM2D) solutions, respectively. The wavefield components: (a) v_z and (b) v_x at $[x^1, x^2]=[518.6, 190]$ m; (c) v_z and (d) v_x at $[x^1, x^2]=[460, 790]$ m.

6 CONCLUSIONS

We developed a novel approach to full-wavefield modeling for coupled acoustic/elastic anisotropic media that include complex bathymetric interfaces. Employing the contravariant representation of the stress and stiffness tensors makes it possible to retain the well-known tensorial symmetries in an arbitrary coordinate system. Semianalytic coordinate mapping helps implement a computationally- and memory-efficient numerical approach that enforces the correct boundary conditions and produces the complete wavefield including body and surface waves. The modeling results and comparison with the spectral-element method confirm that the algorithm accurately simulates wavefields even for strongly undulating bathymetric surfaces overlying structurally complex anisotropic media.

7 ACKNOWLEDGMENTS

We thank the sponsors of the Center for Wave Phenomena, whose support made this research possible. We are grateful to Tugrul Konuk (CWP) for many useful discussions.

APPENDIX A - COORDINATE TRANSFORMATION, METRIC TENSOR, AND CHRISTOFFEL SYMBOLS

In a Cartesian coordinate system there is no distinction between covariant, contravariant and mixed tensor components; however, this is not the case for generalized coordinate representations. This appendix provides a mathematical primer for the generalized framework discussed above, including descriptions of the metric tensor, Christoffel symbols, basis transformations, coordinate transformations, and calculus operations performed in generalized coordinates.

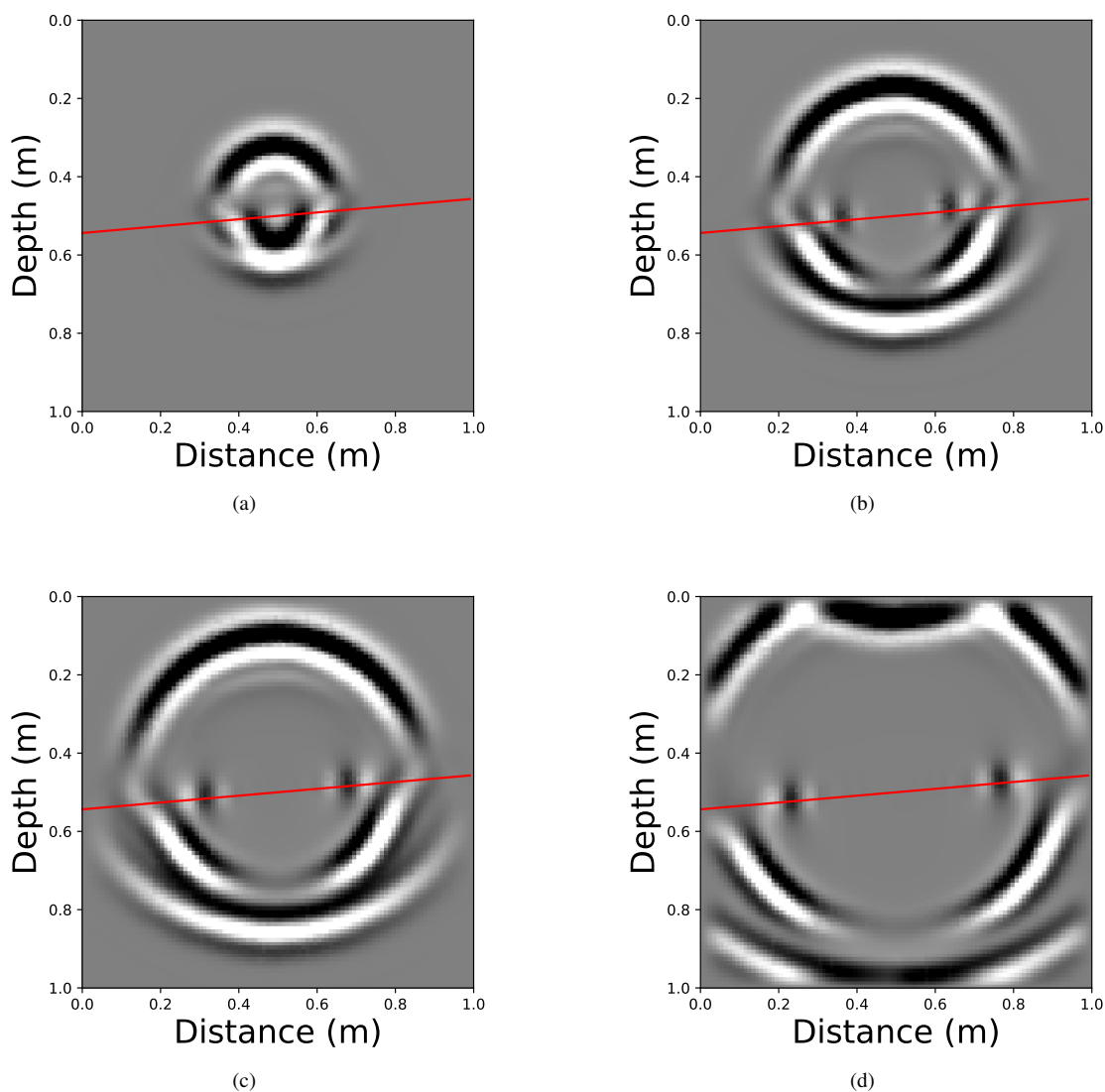


Figure 5. Snapshots of the component v_z at (a) $t=0.15$ s, (b) $t=0.2$ s, (c) $t=0.4$ s, and (d) $t=0.45$ s. The bathymetric surface (red) separates a fluid (top) and a VTI solid (bottom). The VTI medium is defined by $V_{P0} = 1.7$ km/s, $V_{S0} = 1.2$ km/s, $\epsilon = 0.2$, $\delta = 0.1$ and $\rho_S = 1.5$ g/cm³. The velocity and density in the fluid are $c_f = 1.5$ km/s and $\rho_f = 1.0$ g/cm³.

A.1 Metric Tensor and Christoffel Symbols

The metric tensor is a fundamental geometric object that provides a tensor measure of how the local space expands, contracts or shears under a coordinate mapping defined by $\mathbf{x} = \mathbf{x}(\boldsymbol{\xi})$ and $\boldsymbol{\xi} = \boldsymbol{\xi}(\mathbf{x})$, where \mathbf{x} and $\boldsymbol{\xi}$ are the Cartesian and generalized coordinate variables, respectively. The components of the metric tensor g_{ij} in the covariant representation are given by:

$$g_{ij} = \frac{\partial x^k}{\partial \xi^i} \frac{\partial x^k}{\partial \xi^j}. \quad (\text{A.1})$$

The contravariant (or inverse) metric tensor can be computed as:

$$g^{ik} g_{ij} = \delta_j^k. \quad (\text{A.2})$$

In matrix format this operation can be represented through matrix inverse:

$$[g^{ij}] = [g_{ij}]^{-1}. \quad (\text{A.3})$$

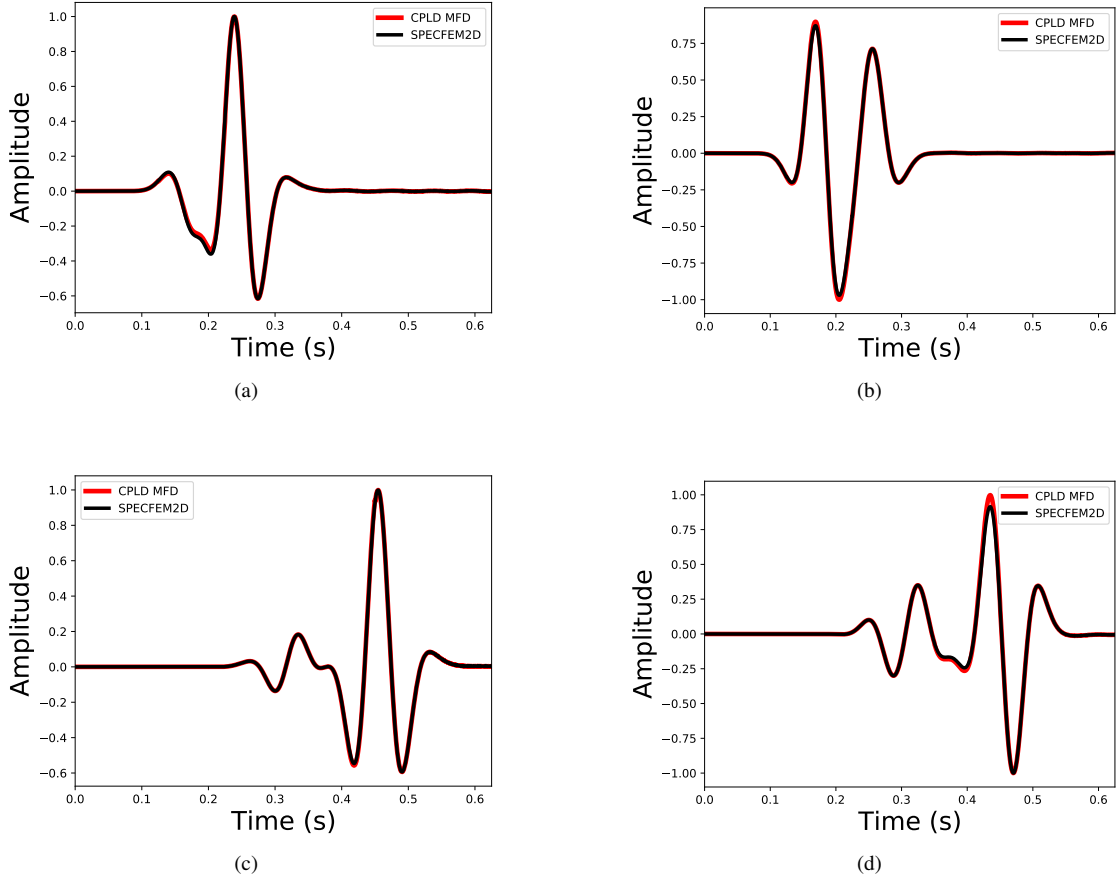


Figure 6. Normalized seismograms for the model in Figure 5. The red and black lines mark the coupled domain MFD (CPLD MFD) and spectral-element (SPECSEM2D) solutions, respectively. The wavefield components: (a) v_z and (b) v_x at $[x,z]=[400,505.2]$ m; (c) v_z and (d) v_x at $[x,z]=[800,470.3]$ m.

The Christoffel symbols Γ_{jl}^i are computed from the metric tensor according to

$$\Gamma_{ij}^k = \frac{1}{2} g^{kl} \left(\frac{\partial g_{li}}{\partial \xi_j} + \frac{\partial g_{lj}}{\partial \xi_i} - \frac{\partial g_{ij}}{\partial \xi_l} \right). \quad (\text{A.4})$$

The partial derivatives in equation A.4 represent tensors measures of the spatial variation of the metric tensor \mathbf{g} . The Christoffel symbols do not formally represent tensors because they do not obey tensor transformation rules but have the symmetries $\Gamma_{kl}^i = \Gamma_{lk}^i$ that are exploited above.

A.2 Basis Transformations

The framework described above requires transformation between contravariant and covariant tensor forms, which can be accomplished through raising and lowering operations. For a rank-one tensor, a contravariant tensor can be obtained from a covariant form via raising the index through contraction with the contravariant metric tensor:

$$f^i = g^{ij} f_j. \quad (\text{A.5})$$

Similarly, we may write the index-lowering operation as:

$$f_i = g_{ij} f^j. \quad (\text{A.6})$$

For rank-two tensors, one may have to apply raising and lowering transformations to both indices.

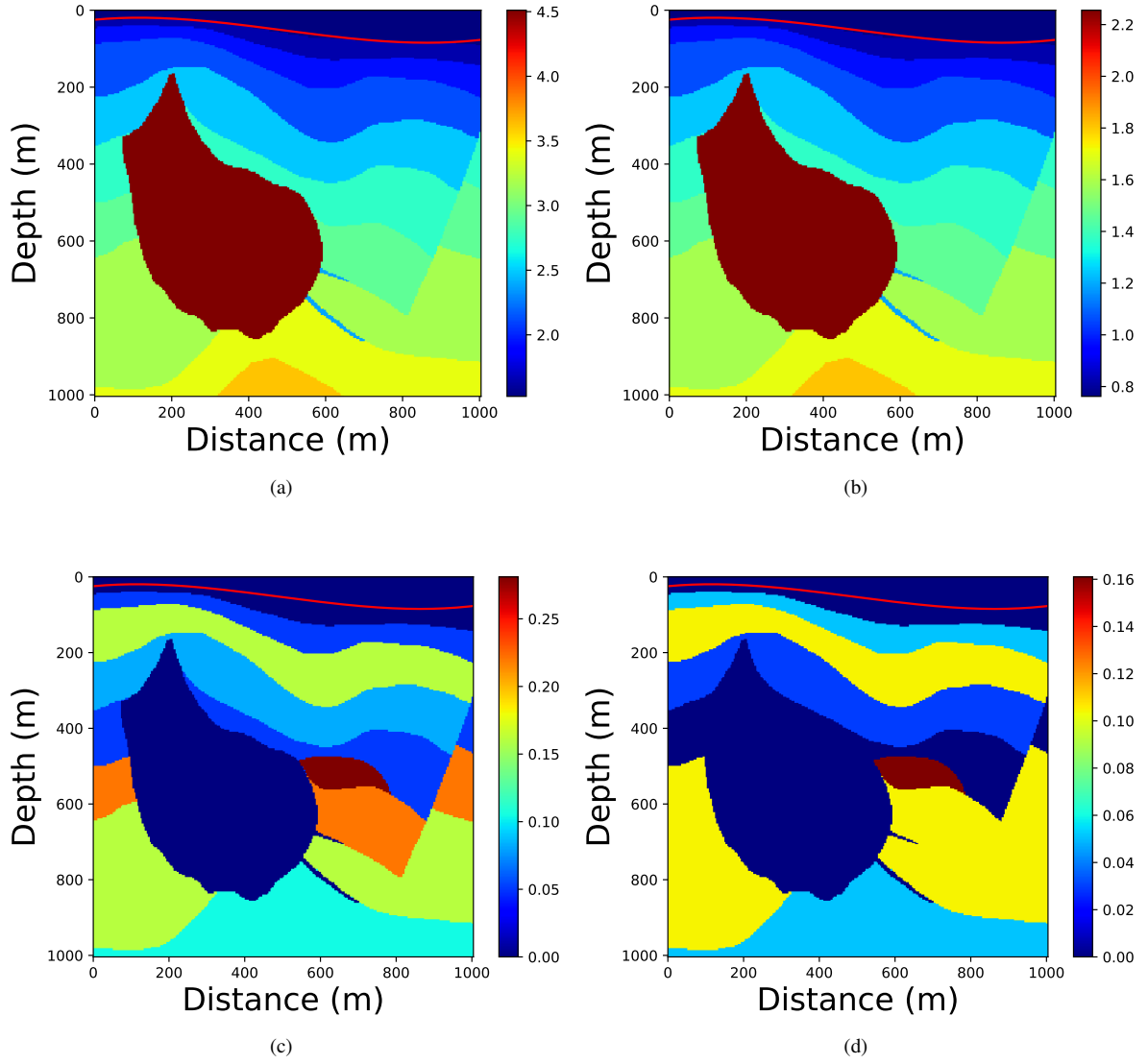


Figure 7. Hess VTI model defined by the Thomsen (1986) parameters (see also Tsvankin, 2012): (a) V_{P0} (in km/s), (b) V_{S0} (in km/s), (c) ϵ , and (d) δ . The red line denotes the bathymetric surface beneath the water layer. The parameters V_{S0} , ϵ , and δ are not defined in the acoustic subdomain, where their values are shown as zeros.

A.3 Coordinate transformations

Switching between the Cartesian and generalized coordinate systems requires implementing a tensor coordinate transformation. Here, we present forward and inverse coordinate transforms between the Cartesian and generalized coordinates for rank-one and rank-two tensors defined in the contravariant basis. The forward transformation of a rank-one tensor from the Cartesian to the generalized coordinates is given by:

$$v^i |_{\xi} = Q_j^i v^j |_{x}, \quad (\text{A.7})$$

where Q_j^i is the following partial derivative that involves both coordinate systems:

$$Q_j^i = \frac{\partial x^i}{\partial \xi^j}. \quad (\text{A.8})$$

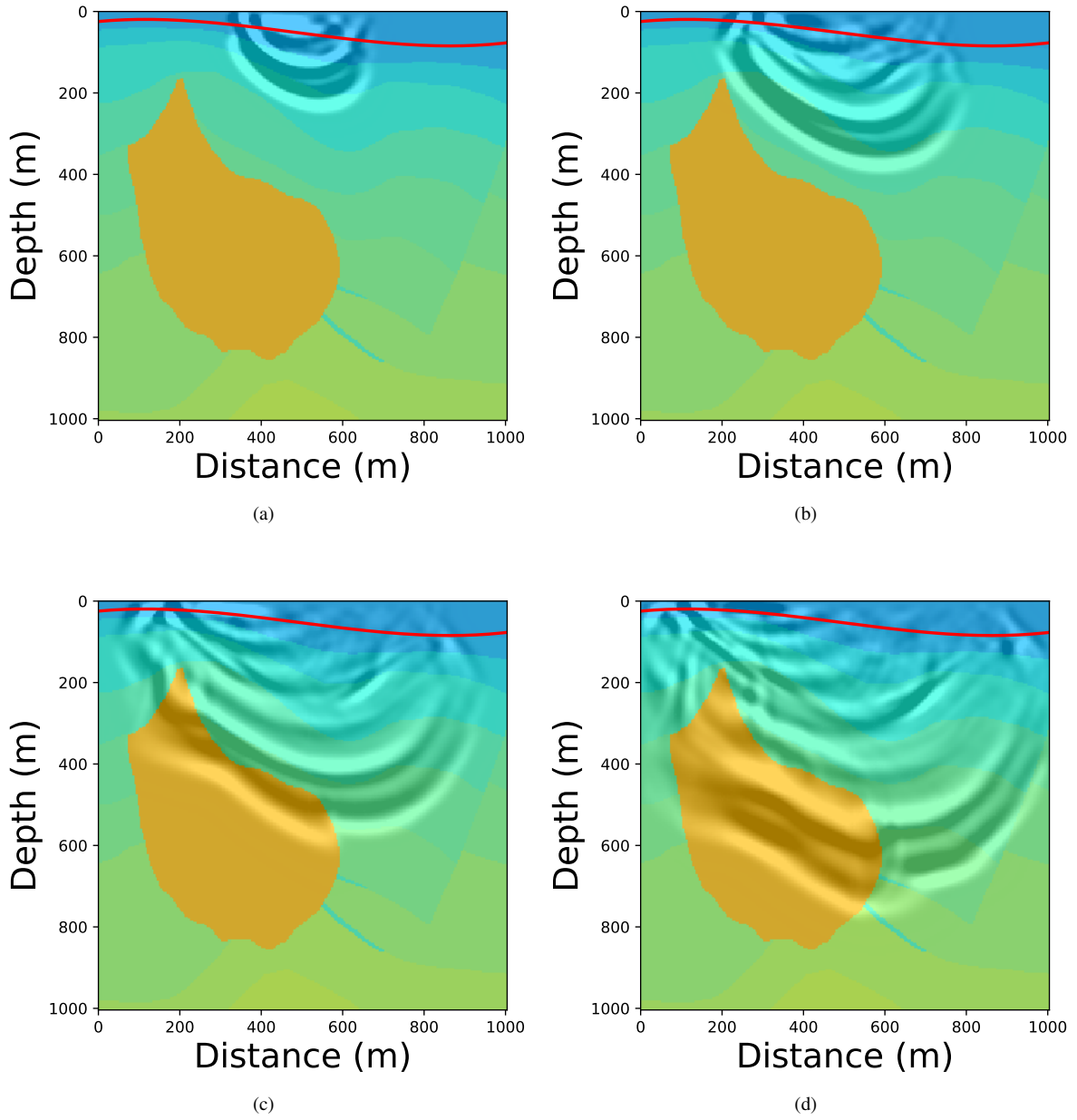


Figure 8. Snapshots of the component v_z for the model from Figure 7. (a) $t=0.15$ s, (b) $t=0.2$ s, (c) $t=0.3$ s, and (d) $t=0.4$ s.

Equation A.8 can be rewritten in matrix form:

$$Q_j^i = \begin{bmatrix} Q_1^1 & Q_2^1 & Q_3^1 \\ Q_1^2 & Q_2^2 & Q_3^2 \\ Q_1^3 & Q_2^3 & Q_3^3 \end{bmatrix}. \quad (\text{A.9})$$

For a rank-one tensor, the inverse coordinate mapping from the generalized to the Cartesian coordinates is defined by:

$$v^j |_{\mathbf{x}} = A_i^j v^i |_{\boldsymbol{\xi}}, \quad (\text{A.10})$$

where the inverse coordinate transformation A_i^j is:

$$A_i^k Q_j^i = \delta_i^k \delta_j^i. \quad (\text{A.11})$$

Similarly, both components of the rank-two tensor σ^{ij} undergo a coordinate transformation according to:

$$\sigma^{kl} |_{\xi} = Q_i^k Q_j^l \sigma^{ij} |_x . \quad (\text{A.12})$$

The inverse coordinate transformation is given by:

$$\sigma^{ij} |_x = A_k^i A_l^j \sigma^{kl} |_{\xi} . \quad (\text{A.13})$$

Similar coordinate transformations can be developed for rank-one and rank-two covariant tensors.

A.4 Calculus operations

In a generalized coordinate system, the contravariant basis vectors \hat{g}^i are unlikely to be orthonormal. Thus, one must define standard calculus operations to account for their geometric variations. The gradient of a scalar field is:

$$\nabla_i \phi = g^{ij} \frac{\partial \phi}{\partial \xi^i} \equiv f^j , \quad (\text{A.14})$$

where f^j denotes the contravariant gradient component in the j th direction. The divergence of a vector field with the contravariant components V^i is:

$$\nabla_i V^i = \frac{\partial V^i}{\partial \xi^i} + \Gamma_{il}^l V^i = \frac{1}{\sqrt{|g|}} \frac{\partial}{\partial \xi^i} \left(\sqrt{|g|} V^i \right) , \quad (\text{A.15})$$

where the second equality is known as the Voyn-Weyl formula. Similarly, the divergence of the second-order contravariant tensor T^{ij} has the form:

$$\nabla_i T^{ij} = \frac{\partial T^{ij}}{\partial \xi^i} + \Gamma_{ik}^i T^{kj} + \Gamma_{ik}^j T^{ik} . \quad (\text{A.16})$$

APPENDIX B - MAPPING EQUATIONS

Here we derive the vertical mapping function that uses quadratic Bézier interpolants to connect three control surfaces: (1) the free surface; (2) the bathymetric profile; and (3) the base of the mesh, which is assumed to be horizontal.

Suppose P_0 , P_1 , and P_2 are the control points, and P_c is the fixed point that the curve passes through. Then the Bezier curve is defined by:

$$x^1 = P(\xi^1) = P_0(1 - \xi^1)^2 + P_1 2(1 - \xi^1)\xi^1 + P_2(\xi^1)^2 , \quad (\text{B.1})$$

where $\xi^1 \in [0, 1]$. There is an infinite number of solutions that might pass through that point for any value of t . Picking one of them (e.g., $\xi^1 = \zeta$), equating this to control point P_c ,

$$P_c |_{\xi^1=\zeta} = P_0(1 - \zeta)^2 + P_1 2\zeta(1 - \zeta) + P_2 \zeta^2 , \quad (\text{B.2})$$

and solving for P_1 yields:

$$P_1 = \frac{P_c - P_0(1 - \zeta^2) - P_2 \zeta^2}{2\zeta(1 - \zeta)} . \quad (\text{B.3})$$

For the problem at hand the control point $P_c = B$ represents the bathymetric surface at the coordinate $\xi^2 = x^2$, $P_0 = 0$ is the water surface, and $P_2 = a$ is the depth where $a > \max(B)$. Introducing these points into equation B.3 results in:

$$P_1 = \frac{B - a\zeta^2}{2\zeta(1 - \zeta)} . \quad (\text{B.4})$$

This means that the 1D mapping function is given by:

$$x^1 = P(\xi^1) = \frac{2(1 - \xi^1)\xi^1(B - a\zeta^2) + 2\zeta(1 - \zeta)a(\xi^1)^2}{2\zeta(1 - \zeta)} . \quad (\text{B.5})$$

After simplifying equation B.5, we get the following expression:

$$x^1 = P(\xi^1) = \frac{\xi^1 (B(\xi^1 - 1) + a\zeta(\zeta - \xi^1))}{\zeta(\zeta - 1)} . \quad (\text{B.6})$$

Note that (1) for the free surface $\xi^1 = 0$, so $x^1 = P(\xi^1) = 0$; (2) at the base of the mesh $\xi^1 = 1$, so $x^1 = P(\xi^1) = a$; and (3) when $\xi^1 = \zeta$, equation B.5 reduces to $P(\zeta) = B$.

Because $\xi^1 \in [0, 1]$, it can be defined numerically on a \mathbf{v} -grid of $N + 1$ points (i.e., from 0 to N) according to:

$$\xi^1 = \frac{n}{N}, \quad 0 \leq n \leq N + 1, \quad (\text{B.7})$$

and an \mathbf{f} -grid with $N + 2$ points by:

$$\xi^1 = \begin{cases} 0 & n = 0; \\ \frac{n - 1/2}{N} & 1 < n \leq N + 1; \\ 1 & n = N + 2. \end{cases} \quad (\text{B.8})$$

REFERENCES

- Appelö, D., and N. A. Petersson, 2009, A stable finite difference method for the elastic wave equation on complex geometries with free surfaces: *Communications in Computational Physics*, **5**, 84–107.
- Brillouin, L., and R. O. Brennan, 1965, *Tensors in mechanics and elasticity*: American Society of Mechanical Engineers Digital Collection.
- Castillo, J. E., and G. F. Miranda, 2013, *Mimetic discretization methods*: Chapman and Hall/CRC.
- Chaljub, E., Y. Capdeville, and J.-P. Vilotte, 2003, Solving elastodynamics in a fluid–solid heterogeneous sphere: a parallel spectral element approximation on non-conforming grids: *Journal of Computational Physics*, **187**, 457–491.
- de Hoop, A. T., and J. H. Van der Hijden, 1984, Generation of acoustic waves by an impulsive point source in a fluid/solid configuration with a plane boundary: *The Journal of the Acoustical Society of America*, **75**, 1709–1715.
- de la Puente, J., M. Ferrer, M. Hanzich, J. E. Castillo, and J. M. Cela, 2014, Mimetic seismic wave modeling including topography on deformed staggered grids: *Geophysics*, **79**, no. 3, T125–T141.
- Flügge, W., 1972, *Tensor analysis and continuum mechanics*: Springer.
- Fornberg, B., 1988, The pseudospectral method: accurate representation of interfaces in elastic wave calculations: *Geophysics*, **53**, 625–637.
- Ge, Z., and X. Chen, 2007, Wave propagation in irregularly layered elastic models: a boundary element approach with a global reflection/transmission matrix propagator: *Bulletin of the Seismological Society of America*, **97**, 1025–1031.
- Hestholm, S., and B. Ruud, 1994, 2d finite-difference elastic wave modelling including surface topography 1: *Geophysical Prospecting*, **42**, 371–390.
- Käser, M., and M. Dumbser, 2008, A highly accurate discontinuous Galerkin method for complex interfaces between solids and moving fluids: *Geophysics*, **73**, no. 3, T23–T35.
- Komatitsch, D., C. Barnes, and J. Tromp, 2000, Wave propagation near a fluid-solid interface: A spectral-element approach: *Geophysics*, **65**, 623–631.
- Komatitsch, D., F. Coutel, and P. Mora, 1996, Tensorial formulation of the wave equation for modelling curved interfaces: *Geophysical Journal International*, **127**, 156–168.
- Komatitsch, D., and J. Vilotte, 1998, The spectral-element method: an efficient tool to simulate the seismic response of 2D and 3D geological structures: *Bulletin of the Seismological Society of America*, **2**, no. 2, 368–398.
- Konuk, T., and J. Shragge, 2019, 3d tensorial elastodynamics for anisotropic media, *in* SEG Technical Program Expanded Abstracts 2019: Society of Exploration Geophysicists, 3934–3938.
- Lisitsa, V., and D. Vishnevskiy, 2010, Lebedev scheme for the numerical simulation of wave propagation in 3D anisotropic elasticity: *Geophysical Prospecting*, **58**, 619–635.
- Martin, R., D. Komatitsch, and S. D. Gedney, 2008, A variational formulation of a stabilized unsplit convolutional perfectly matched layer for the isotropic or anisotropic seismic wave equation: *Computer Modeling in Engineering & Sciences*, **37**, 274–304.
- McConnell, A. J., 2014, *Applications of tensor analysis*: Courier Corporation.
- Padilla, F., M. de Billy, and G. Quentin, 1999, Theoretical and experimental studies of surface waves on solid–fluid interfaces when the value of the fluid sound velocity is located between the shear and the longitudinal ones in the solid: *The Journal of the Acoustical Society of America*, **106**, 666–673.
- Shragge, J., 2017, Tensorial elastodynamics for isotropic media on vertically deformed meshes, *in* SEG Technical Program Expanded Abstracts 2017: Society of Exploration Geophysicists, 4034–4038.
- Shragge, J., and T. Konuk, 2020, Tensorial elastodynamics for isotropic media: *Geophysics*, **85**, no. 6, T359–T373.

- Shragge, J., and B. Tapley, 2017, Solving the tensorial 3D acoustic wave equation: A mimetic finite-difference time-domain approach: *Geophysics*, **82**, T183–T196.
- Singh, H., J. Shragge, and I. Tsvankin, 2021, Mimetic finite-difference coupled-domain solver for anisotropic media: *Geophysics*, **86**, no. 1, T45–T59.
- Sun, Y.-C., W. Zhang, J.-K. Xu, and X. Chen, 2017, Numerical simulation of 2-D seismic wave propagation in the presence of a topographic fluid–solid interface at the sea bottom by the curvilinear grid finite-difference method: *Geophysical Journal International*, **210**, 1721–1738.
- Tarrass, I., L. Giraud, and P. Thore, 2011, New curvilinear scheme for elastic wave propagation in presence of curved topography: *Geophysical Prospecting*, **59**, 889–906.
- Tessmer, E., D. Kosloff, and A. Behle, 1992, Elastic wave propagation simulation in the presence of surface topography: *Geophysical Journal International*, **108**, 621–632.
- Thomsen, L., 1986, Weak elastic anisotropy: *Geophysics*, **51**, 1954–1966.
- Van Vossen, R., J. O. Robertsson, and C. H. Chapman, 2002, Finite-difference modeling of wave propagation in a fluid–solid configuration: *Geophysics*, **67**, 618–624.
- Voinovich, P., A. Merlen, E. Timofeev, and K. Takayama, 2003, A Godunov-type finite-volume scheme for unified solid-liquid elastodynamics on arbitrary two-dimensional grids: *Shock Waves*, **13**, 221–230.
- Wilcox, L. C., G. Stadler, C. Burstedde, and O. Ghattas, 2010, A high-order discontinuous Galerkin method for wave propagation through coupled elastic–acoustic media: *Journal of Computational Physics*, **229**, 9373–9396.
- Zhang, J., 2004, Wave propagation across fluid–solid interfaces: a grid method approach: *Geophysical Journal International*, **159**, 240–252.
- Zhang, W., and X. Chen, 2006, Traction image method for irregular free surface boundaries in finite difference seismic wave simulation: *Geophysical Journal International*, **167**, 337–353.